Alignment Maps of Tissues: II. Fast Harmonic Analysis for Imaging

Theodore T. Tower and Robert T. Tranquillo

Department of Chemical Engineering & Materials Science, University of Minnesota, Minneapolis, Minnesota 55455 USA

ABSTRACT A methodology for generating polarized light retardation and alignment direction images is presented. A rotated quarter-wave plate changes the linear polarized light to a polarized probe with various degrees of ellipticity by which samples are imaged with the use of a circular analyzer. A harmonic representation of image intensity allows simple analysis, requiring only simple image operations and realizing four orders-of-magnitude computational savings for strongly aligned tissues, where linear birefringence is the dominant optical property. The method is demonstrated for a porcine heart valve leaflet.

INTRODUCTION

In many soft connective tissues, the mechanical properties are influenced by fiber alignment. The ability to efficiently generate alignment maps would be a valuable tool in studying the biomechanics of normal, developing, and healing native tissues and artificial tissues. However, generating alignment maps with the commonly used methods of polarized light can be complicated because the optical properties of tissues may include scattering characteristics as well as linear and circular birefringence and dichroism.

In traditional polarization microscopy and orientational spectroscopy, several techniques have been used to determine birefringent and dichroic properties. They can be categorized into methods using a rotating analyzer, retardation compensation, sample rotation, or polarization probe variation (Fuller, 1990). In all cases, information is elucidated about how the sample transforms the incident polarization vector. Using the Mueller calculus, this transformation can be represented by the elements of the sample's Mueller matrix. Although the concept of varying the polarization probe is not new in orientational spectroscopy, few have expanded it to imaging. Bustamante and co-workers developed a formal treatment for generating images of each of the sample's Mueller matrix elements using several static probes and analyzers (Kim 1987). Although their imaging theory is useful, the variety of analyzers and polarizers needed for Mueller-element image generation is somewhat cumbersome. Oldenbourg and Mei (1995) used two variable liquid crystal retarders to render retardation and alignment direction images rapidly via simple image operations and a quadratic approximation of the intensity function. Although the technique is simple and powerful and appropriate for commercialization, the equipment cost may be prohibitive for the general researcher. Another modulation technique

similar to that described herein is a rotating polarizer method, which also does not require sophisticated equipment and uses similar harmonic analysis (Glazer, 1996; Geday, 1900). Consequently, we attempt to broaden the general use of simple polarization modulation techniques that can be readily adopted in the laboratory.

Recently, we described a method to generate retardation and alignment-direction images by nonlinear regression of an exponential Mueller matrix (Tower and Tranquillo, 2001). With the use of a matched isotropic sample, the model corrects for biases due to scattering and circular optical properties that affect the measured linear birefringence. The optical setup required only a rotating $\lambda/4$ plate after the polarizer, to act as a polarization state generator as described by Hauge (1978), and a circular analyzer. Although the optical setup is simple, the analysis is computationally intensive.

We report here that our method can be simplified and the computational cost dramatically reduced when linear birefringence dominates the optical behavior due to strong alignment of collagen fibers that commonly exists in soft connective tissue (e.g., tendon, ligaments, etc.). In these cases, the image intensity can be reformulated in terms of four Fourier coefficient images. These images are directly related to the sample's Mueller matrix from which the linear birefringence or other optical properties can easily be calculated with simple image operations. This method is not only simple and computationally fast, it determines quantities directly related to linear retardation on a pixel-wise basis, and is thus a true imaging method.

We first present the theory of the method, including approximation of the sample's birefringence image and calibration. Use of a Brace-Köhler compensator of fixed retardation to verify the method is then described. As a demonstration, we determined the alignment images (direction and magnitude of retardation) of a fixed porcine aortic heart valve leaflet that exhibits strong and spatially varying alignment (Sauren, 1980). Tissues are optically and structurally complex and thus provide an excellent demonstration of our method.

THEORY

The optic train in Fig. 1 is modeled using Mueller matrix formalism. Unless noted otherwise, matrices are in bold
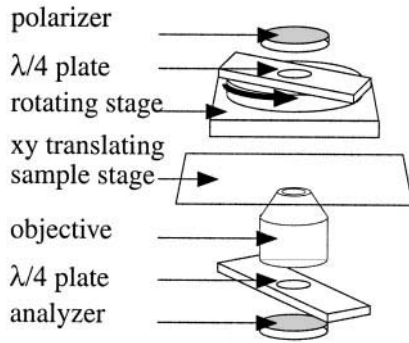

FIGURE 1   Optic train diagram.

upper case letters, vectors in bold lower case letters, and scalar quantities, including images, in italics. Letter subscripts are optic component references, and number subscripts refer to a matrix or vector element. The 4×4 Mueller matrices for the analyzer aligned at $0°$, $\mathbf{P}(0°)$, and polarizer aligned at $90°$, $\mathbf{P}(90°)$, are given by

$$\mathbf{P}(0°) = \begin{bmatrix} 1 & 1 & 0 & 0 \\ 1 & 1 & 0 & 0 \\ 0 & 0 & 0 & 0 \\ 0 & 0 & 0 & 0 \end{bmatrix} \quad \mathbf{P}(90°) = \begin{bmatrix} 1 & -1 & 0 & 0 \\ -1 & 1 & 0 & 0 \\ 0 & 0 & 0 & 0 \\ 0 & 0 & 0 & 0 \end{bmatrix}. \tag{1}$$

The Mueller matrix for a linear birefringent element, $\mathbf{M}_{LB}$, for a given slow axis alignment, α, and retardation, ϕ, is given by

$$\mathbf{M}_{LB}(\alpha, \phi) = \begin{bmatrix} 1 & 0 & 0 & 0 \\ 0 & \cos^2 2\alpha + \cos\phi \sin^2 2\alpha & (1 - \cos\phi)\sin 2\alpha \cos 2\alpha & \sin\phi \sin 2\alpha \\ 0 & (1 - \cos\phi)\sin 2\alpha \cos 2\theta & \sin^2 2\theta + \cos\phi \cos^2 2\theta & -\sin\theta \cos 2\alpha \\ 0 & -\sin\phi \sin 2\alpha & \sin\phi \cos 2\alpha & \cos\phi \end{bmatrix}. \tag{2}$$

Each matrix modifies the polarization of the incident light, characterized by the Stokes vector, $s = [s_0, s_1, s_2, s_3]^T$. By convention, s_0 is the intensity of the light, and s_1, s_2, and s_3 are the $0°/90°$ linear component, $45°/-45°$ linear component, and the right/left circular component, respectively. We multiply the incoming light vector by the model Mueller matrix for each element light traverses, until we generate the complete optic train model,

$$\mathbf{P}(0°)\mathbf{M}_{LB}(\alpha_f, \phi_f)\mathbf{M}\mathbf{M}_{LB}(\alpha_r + \theta, \phi_r)\mathbf{P}(90°)s_i = s_o, \tag{3}$$

where s_i and s_0 are the Stokes vectors describing incident, unpolarized light and resultant, linearly polarized light, respectively, θ is the rotation angle of the $\lambda/4$ plate, and the subscripts r and f refer to the rotating and the fixed $\lambda/4$ plates, respectively. $\mathbf{M}$ is the general Mueller matrix for the sample. The measurable quantity is the total intensity (i.e., light that is not extinguished by the analyzer), i, which is the first element of s_0, as a function of rotation angle.

For simplification, we combine the matrices before and after $\mathbf{M}$ in Eq. 3, including s_i, which yields an elliptical analyzer matrix, $\mathbf{K}$, and a probe light vector, $\mathbf{s}_{probe}$, whose polarization state is determined by the rotation of the $\lambda/4$ plate. $\mathbf{K}$ represents all elliptical analyzers, including the special cases of linear and circular analyzers. Given $\mathbf{P}(0°)$, the perfect horizontal analyzer from Eq. 2, the first two rows of $\mathbf{K}$ are identical, and the last two rows are zero. The intensity, i, may thus be calculated by replacing $\mathbf{K}$ with the row vector, $\mathbf{k}$, the first row of $\mathbf{K}$. The two vectors, $\mathbf{k}$ and $\mathbf{s}_{probe}$, representing the general elliptical analyzer and the probe light vector, are then as

$$\mathbf{k} = \mathbf{K}_{1i,i=1,4} = (\mathbf{P}(0°)\mathbf{M}_{LB}(\alpha_f, \phi_f))_{1i,i=1,4}$$

$$= \begin{pmatrix} 1 \\ \cos^2\left(\dfrac{\phi_f}{2}\right) + \sin^2\left(\dfrac{\phi_f}{2}\right)\cos(4\alpha_f) \\ \sin^2\left(\dfrac{\phi_f}{2}\right)\sin(4\alpha_f) \\ \sin(\phi_f)\sin(2\alpha_f) \end{pmatrix}, \tag{4}$$

$$\mathbf{S}_{probe} = \mathbf{M}_{LB}(\alpha_r + \theta, \phi_r)\mathbf{P}(90°)\mathbf{s}_i$$

$$= \begin{pmatrix} 1 \\ -\cos^2\left(\dfrac{\phi_r}{2}\right) - \sin^2\left(\dfrac{\phi_r}{2}\right)\cos(4(\theta + \alpha_r)) \\ -\sin^2\left(\dfrac{\phi_r}{2}\right)\sin(4(\theta + \alpha_r)) \\ \sin(\phi_r)\sin(2(\theta + \alpha_r)) \end{pmatrix}. \tag{5}$$

Finally, Eq. 3 can be rewritten in terms of measured intensity in simplified form as

$$i = \mathbf{k}\mathbf{M}\mathbf{s}_{probe}. \tag{6}$$

Harmonic image analysis

We define an intensity image, I, from the measured intensities, i, at each pixel given by Eq. 6. It can be shown that the intensity defined by Eq. 6 can be represented by a constant term, a term dependent on 2θ, and two on 4θ (for a similar formulation see Collett, 1993). With no loss of generality, I can be expressed as the sum of four images:

$$I = A + B\cos(4(\theta + \alpha_r))$$
$$+ C\sin(4(\theta + \alpha_r)) + D\sin(2(\theta + \alpha_r)). \tag{7}$$

Note that I is a truncated, but exact, Fourier series. Using the orthogonality property of the trigonometric functions in

Eq. 7, the Fourier coefficient images A, B, C, and D in Eq. 7, which contain the Fourier coefficient values at each pixel location, are determined as shown in Eq. 8, where n is the number of evenly spaced images acquired over 180°.

$$
\begin{aligned}
A &= \frac{1}{n}\int_0^\pi I(\theta)\,d\theta \\
&\approx \frac{1}{n}\sum_{i=1}^n I(\theta_i), \\
B &= \frac{2}{n}\int_0^\pi I(\theta)\cos(4(\theta_i + \alpha_r))\,d\theta \\
&\approx \frac{2}{n}\sum_{i=1}^n I(\theta_i)\cos(4(\theta_i + \alpha_r)), \\
C &= \frac{2}{n}\int_0^\pi I(\theta)\sin(4(\theta_i + \alpha_r))\,d\theta \\
&\approx \frac{2}{n}\sum_{i=1}^n I(\theta_i)\sin(4(\theta_i + \alpha_r)), \\
D &= \frac{2}{n}\int_0^\pi I(\theta)\sin(2(\theta_i + \alpha_r))\,d\theta \\
&\approx \frac{2}{n}\sum_{i=1}^n I(\theta_i)\sin(2(\theta_i + \alpha_r)).
\end{aligned}
\tag{8}
$$

These coefficient images are the constant and periodic components of I. Rearrangement of the image form of the intensity equation (Eq. 6) allows us to combine the Fourier coefficient images of I and the constant parts of the rotating $\lambda/4$ plate retardation terms of s_{probe} to define the four elements of the analyzer-sample product, kM:

$$
\begin{aligned}
(kM)_1 &= A - \frac{B}{\tan^2(\phi_r/2)}, \\
(kM)_2 &= -\frac{B}{\sin^2(\phi_r/2)}, \\
(kM)_3 &= -\frac{C}{\sin^2(\phi_r/2)}, \\
(kM)_4 &= \frac{D}{\sin(\phi_r)}.
\end{aligned}
\tag{9}
$$

These four images are completely general with respect to the type of analyzer and form of M. Different analyzers extract different portions of M, and the addition of a rotating

$\lambda/4$ plate after the sample allows determination of all 16 elements of M (Hauge, 1978). Using a fixed-position elliptical analyzer, four independent analyzer-sample images are generated, restricting analysis to sample models with four or fewer unknowns. Assuming that the sample acts as a linear birefringent element, with a characteristic alignment direction, χ, and retardation, δ, being the two unknowns at each pixel, these four independent images can be analyzed to yield alignment direction and retardation images, as described in the next section.

Determination of sample birefringence

For an ideal left circular analyzer, $k = [1, 0, 0, 1]$ and $kM = [M_{11} + M_{41}, M_{12} + M_{42}, M_{13} + M_{43}, M_{14} + M_{44}]$. Assuming that the sample acts as a linear birefringent element, Eq. 2 describes M. Then, the kM vector has the form,

$$
kM = [1 - \sin\delta\,\sin 2\chi \quad \sin\delta\,\cos 2\chi \quad \cos\delta]
\tag{10}
$$

One can see that the retardation, δ, can be calculated from $(kM)_4$ and the alignment direction, α_s, can be calculated from $(kM)_2$ and $(kM)_3$. However, in general, the second and third elements of k may not be zero, and the calculation of χ and δ is more complex. For the realistic case of an elliptical analyzer (where k is given by Eq. 4), the analytical expression for χ is

$$
\chi = \tfrac{1}{2}\tan^{-1}((kM)_2 - k_2, (kM)_3 - k_3),
\tag{11}
$$

where kM and k are normalized by the magnitude of their harmonic components,

$$
\sqrt{\sum_{i=2,4}(kM)_i^2} \quad \text{and} \quad \sqrt{\sum_{i=2,4}k_i^2},
$$

respectively.

The analytical expression for δ is more complex, but δ is easily determined numerically. From Eq. 10, $(kM)_4$ is $\cos\delta$ for an ideal circular analyzer, which yields a good initial guess, δ^0, for the potentially imperfect circular (i.e., elliptical) analyzer described by $K = P(0)M_{LB}(\alpha_f, \phi_f)$. The Newton Raphson algorithm was applied to $(kM)_4$ with the residual defined as

$$
\begin{aligned}
F(\delta) = &-(kM)_4 + k_2\sin\delta\,\sin 2\chi \\
&- k_3\sin\delta\,\cos 2\chi + k_4\cos\delta.
\end{aligned}
\tag{12}
$$

Because all the quantities here are calculated independent of their location in an image, all scalar quantities can be calculated via image operations in a process referred to as overloading (i.e., applying functions that can operate on scalars, vectors, and matrices). The entire scheme then is a series of simple image operations that result in a rapid least-squares regression fit for δ and χ on a pixel basis, yielding alignment retardation and direction images, Δ and X, of the sample.

For verification, we determined the alignment retardation and direction for a Brace-Köhler compensator aligned in different directions. The Vernier dial on the compensator was rotated in 10° increments from where the Maltese cross was observed in the back focal plane.

Statistical significance

The significance of the alignment direction and retardation was calculated using the analysis of variance F-test. Because all of the alignment information is contained within the harmonic component images, $(\mathbf{kM})_{2-4}$, these provide a basis for determining the alignment significance. The hypothesis that a given pixel location has significant alignment was tested against the null hypothesis that the harmonic components for that pixel are not statistically different from when there was no sample present. For the F-test, the harmonic components at each pixel were scaled by the sample's harmonic magnitude at that pixel $(\sqrt{\sum_{i=2,4} (\mathbf{kM})_i^2})$.

Sum of squares of errors (SSE) images were calculated for both the isotropic (null hypothesis) and aligned model (tested hypothesis) and an F-statistic image, F, was generated using Eq. 13. From F, a binary image was generated, showing all parts of the sample that demonstrated measurable retardation with a significance level better than 10^{-3}.

$$F = \frac{\text{change in SSE/number of parameters tested}}{\text{variability of model}}$$

$$= \frac{(\text{SSE}_i - \text{SSE}_a)/df_t}{\text{SSE}_a/df_{\text{error}}}, \qquad (13)$$

where SSE_i and SSE_a are the sum of squares of errors images for the isotropic and aligned models, respectively, and df_t and df_{error} are the degrees of freedom for the number of tested parameters in the model (three, testing the harmonic components $(\mathbf{kM})_{2-4}$) and the unexplained error ($n - 4$, where n is the number of images acquired), respectively.

Birefringence approximation

In addition to the extensive quantity of retardation, one can get an approximation of the intensive birefringence by having an estimate of the number of linear birefringent elements in the sample per unit area (assuming that the sample is homogenous through the thickness). The average intensity image, A, from Eq. 8 and a blank field are used to obtain an approximation to the optical density image, and therefore the total amount of absorbers per area. If the absorbers are the birefringent material, then the retardation can be normalized by the total amount of absorbers to create an approximation of the birefringence image.

The maximum intensity of the average intensity image, $\max(A)$, occurs where there is the minimum amount of absorbing species present. The optical density image is then $\text{OD} = \max(A) - A$. Assuming the optical density follows the Beer–Lambert Law, then $\text{OD} = e^{-kcl}$, where k is the absorption coefficient, c is the concentration of the absorbing species, and l is the path length. The quantity of interest is the total absorbers per area, $cl - \ln(\text{OD})$ is thus proportional to the total number of absorbers and, by assumption, the amount of retarding material. The proportional birefringence image, $\tilde{\Delta}$, is then

$$\tilde{\Delta} \propto - \Delta/\ln(\text{OD}). \qquad (14)$$

Calibration

The alignment (α_f) and retardation (ϕ_f) of the fixed $\lambda/4$ plate can be determined from blank intensity data modeled with Eq. 15, because, for a blank, $\mathbf{M}$ is the identity matrix, $\mathbf{I}$,

$$i = \mathbf{kIs}_{\text{probe}}. \qquad (15)$$

The scalar Fourier coefficients, $[a, b, c, d]$, determined from i can be rearranged as before to yield the four elements of the general analyzer vector, $\mathbf{k}$. Elements k_2 and k_3 of Eq. 4 can be used to solve for α_f and ϕ_f, resulting in

$$\alpha_f = \frac{1}{4} \cos^{-1}\left(\frac{k_3^2 - (k_2 - 1)^2}{k_3^2 + (k_2 - 1)^2}\right) \qquad (16)$$

and

$$\phi_f = 2 \cos^{-1} \sqrt{\frac{1 + k_2 + k_3^2/(k_2 - 1)}{2}}. \qquad (17)$$

The alignment (α_r) and retardation (ϕ_r) of the rotating $\lambda/4$ plate can be determined from the blank and reference (Brace-Köhler compensator) intensity data, respectively. A Fourier representation consisting of $\cos 2\theta$, $\sin 2\theta$, and constant terms describes the light intensity profile of the rotating $\lambda/4$ plate with no sample. From the coefficients of the periodic terms, one can easily determine α_r. Then, using the intensity curve of the reference, ϕ_r is iteratively changed until ϕ agrees with the known reference retardation.

MATERIALS AND METHODS

Experiments were performed on a research-grade Olympus IX-70 inverted light microscope equipped with the following features: brightfield optics (4×, 10×, and 20× objectives, with 1.5× additional attachment), side-port mounted Photometrics SenSYS CCD digital camera (1317 × 1035 pixels, 12-bit grayscale, SCSI interface), halogen source, and monochromatic filter (546 nm). A motorized X-Y translating stage (Ludl), a rotating stage(Oriel), and light shutters were controlled by a Ludl Electronic Products MAC 2000 controller. The Inovision dsp/os software running on a Silicon Graphics O_2 provided direct control of image acquisition and sample positioning through operating-system-level commands accessed via custom Perl scripts.

Figure 1 shows the schematic for the microscope optic train. All angles are relative to the fixed analyzer. The halogen light source is followed by a monochromatic filter (546 nm), a polarizer aligned at 90°, and a $\lambda/4$ plate

TABLE 1 Calculated χ and δ for a Brace-Köhler compensator

χ			δ
Estimated	Calculated	ϵ_χ	Calculated[‡]
0	−2.75	2.75	8.23
9.62	7.20	2.41	8.17
19.23	17.12	2.11	8.15
28.85	27.11	1.73	8.10
38.46	37.52	0.94	8.06
48.07	47.30	0.78	7.94
57.69	57.66	0.04	7.94
67.31	68.16	−0.85	7.93
76.92	78.84	−1.92	7.93
86.54	89.34	−2.80	8.14

*Estimated angle of Vernier based on manual setting.
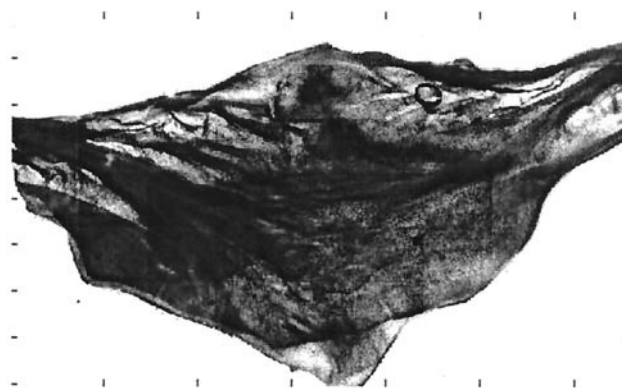[†]Calculated using Eq. 11.
[‡]Calculated using Eq. 12.

FIGURE 2 Brightfield image of a porcine heart valve leaflet. The top edge is the free edge of the leaflet and the bottom edge attaches to the aortic root. The dark bands near the top are highly organized collagen bundles extending into the belly of the leaflet.

(slow axis at 45°) mounted to the motorized rotating stage. The sample was placed on the motorized X-Y stage. A second $\lambda/4$ plate (slow axis at 45°) was inserted in the body slot beneath the objective, followed by the analyzer.

The samples used for verification and demonstration of the method were a Brace-Köhler compensator and a porcine heart valve leaflet fixed in 4% glutaraldehyde. Images were acquired using the Photometrics Sensys CCD camera as described previously (Tower and Tranquillo, 2001). The quarter-wave plate was rotated to 15 positions evenly spaced over 180°. At each rotation position, an image was acquired at 200-ms exposure and 3×3 pixel binning at $4\times$ magnification in a raster fashion to generate a mosaic that would encompass the sample (a 9×12 image mosaic for the heart valve described within). The image mosaics were subsequently reduced to $^{1/10}$/ size so the final working images were 260×160 pixels. Image operations were performed in MATLAB (version 5.2.0, Mathworks, Inc.) with the Image Processing Toolbox. Vector maps were generated by averaging the retardation and direction images over $n \times n$ pixels, where n is a user-defined binning size that determines the vector plot resolution.

RESULTS

Verification of the method

The calculated alignment direction and retardation of a Brace-Köhler compensator are listed in Table 1. The calculated retardation did not significantly vary with direction. The mean calculated retardation was 8.06° ($\sigma = 0.12$). The error between the vernier angle and the calculated theta is most likely due to human error in adjusting the dial, especially given the systematic variation of the error. The corresponding retardations of the rotating and fixed $\lambda/4$ plate were 78° and 81°, respectively.

Demonstration of the method

The average intensity image, A, of the heart valve leaflet is shown in Fig. 2. The leaflet is oriented such that its free edge is the top edge, with commissures located at both ends of the free edge. The thick collagenous chords are easily seen near the edges.

The alignment of the leaflet was determined from the coefficient images of the Fourier representation. The analyzer-sample images, **kM**, calculated by Eqs. 9 are shown in Fig. 3. The retardation and alignment images, Δ and **X**, determined using Eqs. 11 and 12 are shown in Figs. 4 and 5. The maximum retardation of the image was approximately 120°. The calculated uncertainty errors for Δ and **X** were both under 3° for these images. But, in general, when the sample retardation was under 5°, the uncertainty increased rapidly. The thick collagen fiber bundles projected from the commissures are seen as bright chords in Fig. 4, revealing their high degree of alignment. Almost the entire leaflet exhibited significant alignment as shown by the significance image in Fig. 6, where white pixels represent significance, p, that is better that 0.001. A vector map generated by from the Δ and **X** images is superimposed on the average intensity image shown in Fig. 7. The direction and magnitude of the vectors are the 10×10 pixel averaged local alignment direction and retardation, respectively. The vectors reveal the expected commissure-to-commissure alignment observed in valve leaflets (Sauren, 1980).

The birefringence image was constructed using an effective optical density image (not shown) from the average intensity image, A, and is shown in Fig. 8. The bright chords seen in the retardation image (Fig. 4) become more diffuse as they extend toward the belly of the leaflet, forming a more spatially uniform field.

The fifteen 260×160 pixel images were analyzed in 9.4 Mflops, which, on our workstation, required $\sim$5 s. Using a nonlinear regression block-processing method described previously (Tower and Tranquillo, 2001), determination of a 20×20 vector map took approximately 10 min, meaning that the simplifications possible for strong linear retarders like the leaflet yield a computational savings of four orders of magnitude.
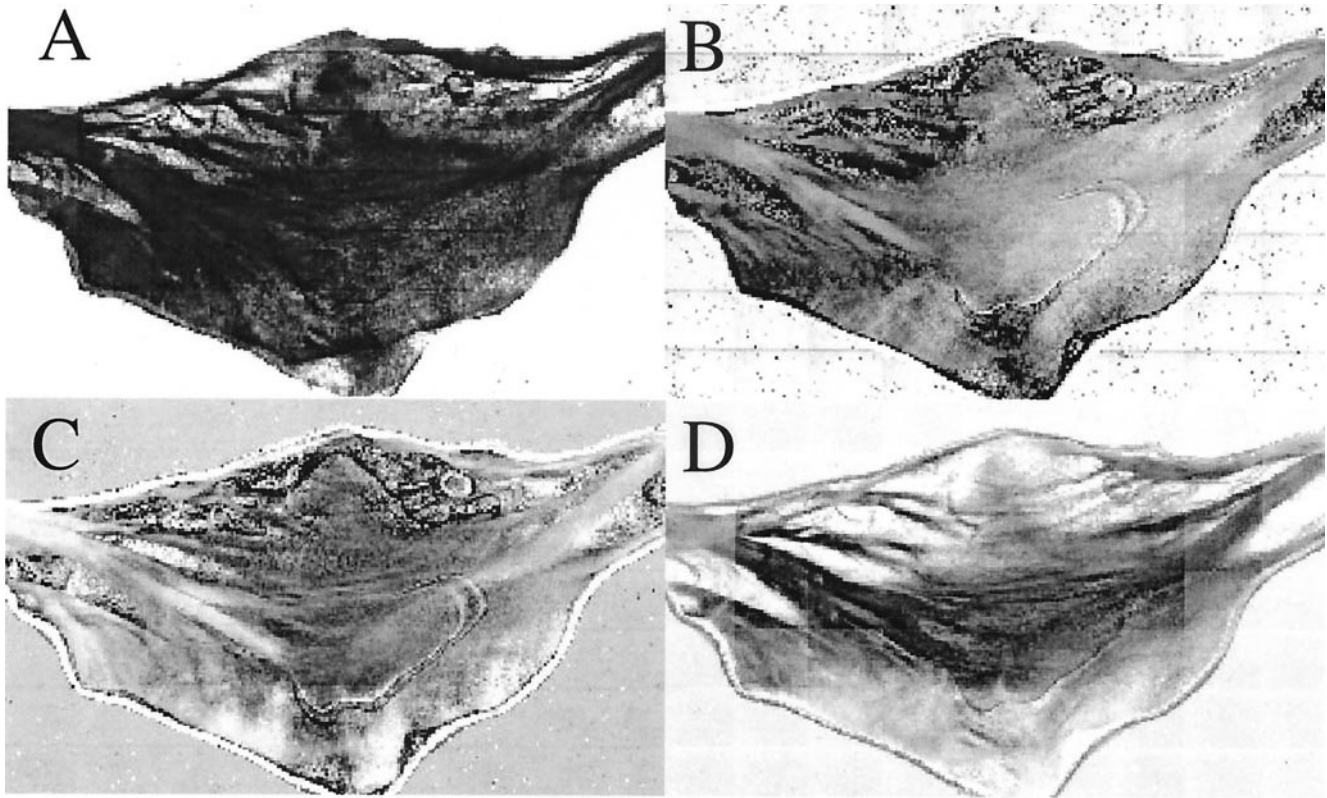
FIGURE 3 The four Fourier coefficient images. (*A*) Average intensity. (*B*) cos 4θ image. (*C*) sin 4θ image. (*D*) sin 2θ image.

SUMMARY

We have presented a novel method to generate alignment direction and retardation images using periodic elliptically polarized illumination. The periodic polarization state of the incident light is easily achieved and implemented by using plane polarized light followed by a rotated λ/4 plate. The image intensity is exactly represented with four Fourier coefficient images that are related to the sample's optical properties. Rearrangement of equations involving these im-

ages yields simple expressions to describe a sample's linear birefringence through its alignment direction image (**X**) and its retardation image (Δ). Although linear birefringence has been the focus of this paper, other expressions may be derived, with the appropriate choice of analyzer, to image other optical properties.

Orientational spectroscopy uses simple and straightforward frequency analysis to determine optical properties. The same methods have been extended here to an imaging
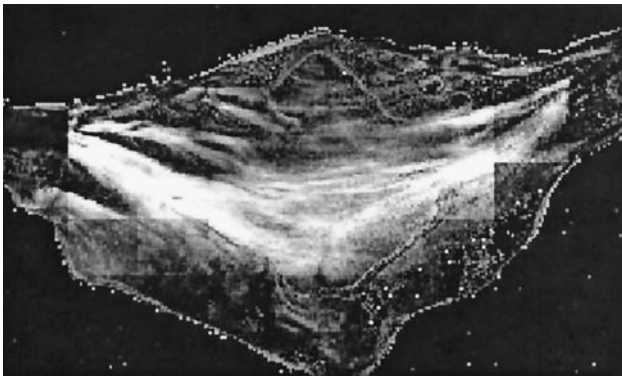

FIGURE 4 Retardation image (Δ). The gray scale is the retardation. The bright chords from the commissures along the aortic root along the top edge are highly aligned bundles of collagen fibers.
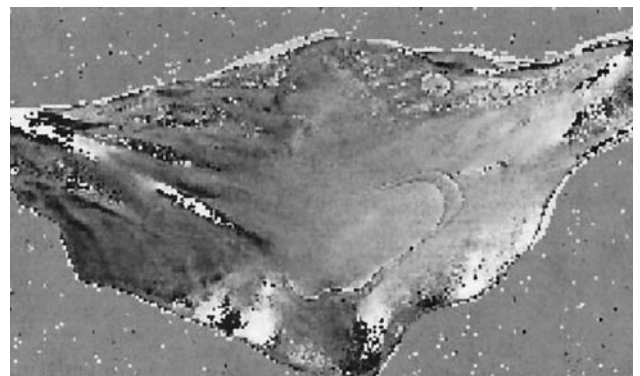

FIGURE 5 Alignment direction image (**X**). The gray levels represent directions from −90° (*white*) to 90° (*black*), with the background gray being 0° (horizontal).
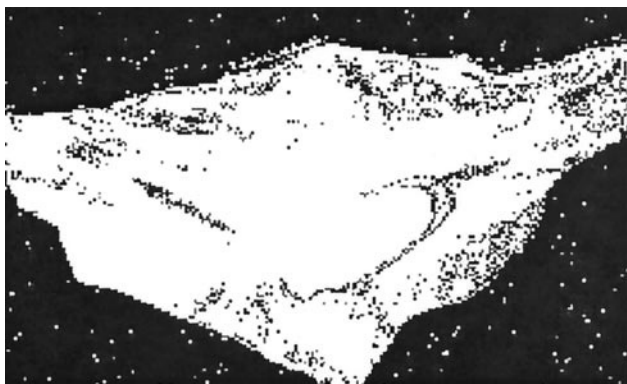
FIGURE 6 Alignment significance image. White pixels denote alignment whose significance is better than $p = 0.001$. For a strongly aligned tissue, such as this leaflet, almost the entire tissue demonstrates significant alignment.

FIGURE 8 Birefringence image. Normalizing the retardation image (R, Fig. 4) by the approximate optical density image (an estimate of the amount of collagen present at each pixel) is proportional to the tissue birefringence. This image reveals areas that have higher or lower alignment per mass. Note that the collagenous chords exhibit a high alignment per mass, while the connective tissue between them exhibits less.

system, allowing the generation of the Fourier coefficient images by simple image operations (e.g., addition, multiplication, and trigonometric functions). Refining the calculations to a series of image operations significantly decreases computational overhead, realizing a computation savings of nearly four orders of magnitude over the nonlinear regression/block processing method described elsewhere (Tower and Tranquillo, 2001).

As shown here and previously (Tower and Tranquillo, 2001), orientational imaging does not require elaborate hardware and system integration (e.g., photoelastic modulators, lock-in amplifiers, etc). Using a rotating $\lambda/4$ plate and a circular analyzer along with simple image processing is sufficient for linear birefringence and may be so for other optical properties. Automation of an *xy* stage or the rotating stage is not inherently necessary, although it does make imaging large samples by image mosaics much easier. Ori-

entational imaging need not be limited by sophisticated hardware integration, which is often the largest hurdle, but rather by existing computational resources, which are constantly improving.

Our method can accurately generate alignment maps for samples that act as linear retarders to within a few degrees of retardation. However, tissues and tissue-equivalents (i.e., constructs fabricated by allowing cultured cells to contract and align networks of collagen fibrils (Barocas et al., 1998)) can exhibit optical properties deviating from a linear retarder such as scattering and circular birefringence (Tower and Tranquillo, 2001). Particularly when high numerical aperture optics are used, polarized scattering effects become important (Tower and Tranquillo, 2001), resulting in inaccurate results for weakly aligned tissue-equivalents (i.e., where $\delta < 10°$). Fortunately, for highly aligned tissues and tissue-equivalents, linear retardation dominates the optical properties.

The heart valve leaflet is an attractive choice of tissue to demonstrate our method because the regions of strong alignment (the collagenous chords) are visually apparent. The birefringence image reveals that these highly aligned collagen-fiber bundles spread out to create a less aligned region in the leaflet belly. This hammock-type architecture agrees with reported observations (Sauren, 1980). This method can be applied to other tissues or other fibrillar structures where linear birefringence is the dominant optical property.

REFERENCES

Barocas, V. H., T. S. Girton, and R. T. Tranquillo. 1998. Engineered alignment in media equivalents: magnetic prealignment and mandrel compaction. *J. Biomech. Eng.* 120:660–666.
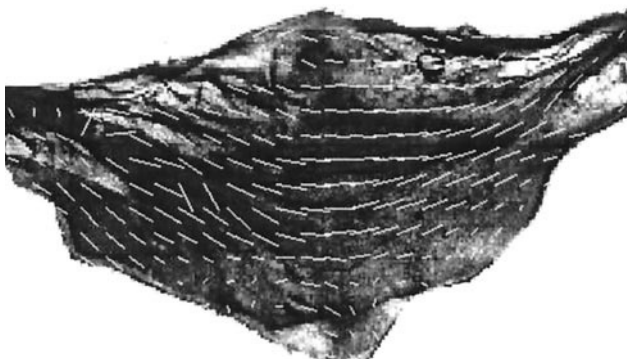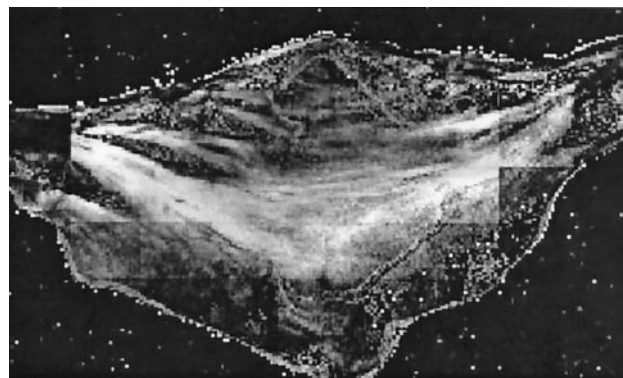

FIGURE 7 Alignment image. The top left and right corners are the heart valve commissures, where this leaflet connected to neighboring leaflets. The lines demonstrate the expected commissure-to-commissure alignment throughout the leaflet. The direction and magnitude of the vectors are the 10×10 pixel averages of the alignment direction and retardation, respectively.

Collett, E. 1993. Polarized Light: Fundamentals and Applications. Marcel Dekker, Inc., New York.

Fuller, G. G. 1990. Optical rheometry. *Annu. Rev. Fluid. Mech.* 22: 387–417.

Geday, M. A., W. Kaminsky, J. G. Lewis, and A. M. Glazer. 2000. Images of absolute retardance $L \cdot \Delta n$, using the rotating polariser method. *J. Microscopy.* 198:1–9.

Glazer, A. M., J. G. Lewis, and W. Kaminsky. 1996. An automatic optical imaging system for birefringent media. *Proc. Roy. Soc. Lond. (A).* 452:2751–2765.

Hauge, P. S. 1978. Mueller matrix ellipsometry with imperfect compensators. *J. Opt. Soc. Am.* 68:1519–1528.

Kim, M., D. Keller, and C. Bustamante. 1987. Differential polarization imaging: I. Theory. *Biophys. J.* 52:911–927.

Oldenbourg, R., and G. Mei. 1995. New polarized light microscope with precision universal compensator. *J. Microscopy.* 180:140–147.

Sauren, A. A. H. J., W. Kuijpers, A. A. van SteenHoven, and F. E. Veldpaus. 1980. Aortic valve histology and its relation with mechanics—preliminary report. *J. Biomech.* 13:97–104.

Tower, T. T., and R. T. Tranquillo. 2001. Alignment maps of tissues: I. Microscopic elliptical polarimetry. *Biophys. J.* 81:2954–2963.